PAPER • **OPEN ACCESS**

Principal component analysis in application to Brillouin microscopy data

To cite this article: Hadi Mahmodi *et al* 2024 *J. Phys. Photonics* **6** 025009

Journal of Physics: Photonics

PAPER

Principal component analysis in application to Brillouin microscopy data

Hadi Mahmodi[1,4], **Christopher G Poulton**[1,4], **Mathew N Leslie**[2], **Glenn Oldham**[3], **Hui Xin Ong**[2], **Steven J Langford**[1] **and Irina V Kabakova**[1,*]

[1] School of Mathematical and Physical Sciences, University of Technology Sydney, NSW, Ultimo, Australia
[2] Respiratory Technology, Woolcock Institute of Medical Research, NSW, Glebe, Australia
[3] Swinburne University of Technology, Melbourne, Victoria, Australia
[4] Equal contributions.
[*] Author to whom any correspondence should be addressed.

E-mail: irina.kabakova@uts.edu.au

Keywords: Brillouin microscopy, principle components, unsupervised learning, hyperspectral data

Supplementary material for this article is available online

OPEN ACCESS

RECEIVED
17 December 2023

REVISED
3 March 2024

ACCEPTED FOR PUBLICATION
20 March 2024

PUBLISHED
28 March 2024

Abstract

Brillouin microscopy has recently emerged as a new bio-imaging modality that provides information on the microscale mechanical properties of biological materials, cells and tissues. The data collected in a typical Brillouin microscopy experiment represents the high-dimensional set of spectral information, i.e. each pixel within a 2D/3D Brillouin image is associated with hundreds of points of spectral data. Its analysis requires non-trivial approaches due to subtlety in spectral variations as well as spatial and spectral overlaps of measured features. This article offers a guide to the application of Principal Component Analysis (PCA) for processing Brillouin imaging data. Being unsupervised multivariate analysis, PCA is well-suited to tackle processing of complex Brillouin spectra from heterogeneous biological samples with minimal *a priori* information requirements. We point out the importance of data pre-processing steps in order to improve outcomes of PCA. We also present a strategy where PCA combined with *k*-means clustering method can provide a working solution to data reconstruction and deeper insights into sample composition, structure and mechanics.

1. Introduction

Brillouin microscopy (BM) is a type of spectroscopic imaging where image contrast relies on the variation of micro-mechanical properties in matter [1–3]. These properties are obtained by direct detection of the speed and attenuation of hypersound waves. As a technology, BM has received a considerable attention in recent years due to advances in mechanobiology and the growing demand for label-free mechanical characterisation of biological materials, tissues and cells in 3D and at the spatial scales relevant to cellular and subcellular processes [4–6].

The data collected in a typical Brillouin imaging experiment consists of a few thousand individual spectra, each representing up to a thousand of points across the frequency range of interest. Therefore, high-dimensionality is one of the common challenges in analysis of Brillouin imaging data [7]. Each Brillouin spectrum demonstrates a set of peaks associated with inelastic scattering of light by hypersound waves inside the material. Solid state and glassy materials have relatively narrow peaks positioned sufficiently far apart, thus line-fitting methods can be straightforwardly applied to localise the peak's position and its full-width at half maximum—the two quantities needed to assess the material's mechanical properties.

In biological matter, Brillouin signals exhibit broad bandwidth and their spectral position is quite close to the Brillouin frequency of water (owing to high hydration content of biomaterials, cells and tissues) [4, 8]. Additionally, biological tissues and cells are heterogeneous across the imaging volumes traditionally employed in BM (a few cubic microns), leading to spectrally overlapping features. Therefore, another

common challenge of Brillouin data analysis is associated with the subtle spectral variations across the data set accompanied by an overlap in spectral signatures of heterogeneous material components.

These reasons make the analysis of Brillouin data collected from biological samples non-trivial, with simple line-fitting routines producing unsatisfactory results and often taking long processing time, not compatible with real-time imaging [7]. On the other hand, the methods common within the hyperspectral imaging community, in particular multivariate techniques such as Principal Component Analysis (PCA), can provide improvements in both the data processing speed and accuracy, thus supporting the translation of BM to medical diagnostics and routine clinical use [9].

As a simple, non-parametric method for extracting useful information from confusing data, PCA is widely employed in various types of analysis, spanning from neuroscience to computer graphics [10]. This approach enables the reduction of a complex data set to a lower dimension, unveiling the sometimes hidden dynamics that frequently underlies it. In fact, PCA is already routinely applied for analysis of hyperspectral data measured in standard Raman scattering experiments [11] and coherent anti-Stokes Raman imaging [12]. Within the Brillouin microscopy community, unsupervised multivariate techniques have so far been under-utilised, with only a few reports published to date [7, 13, 14]. It has been shown that the scores of principal components can be used as markers for classification and sorting pathological samples from healthy tissues [14]. Notably, the highest score principal component (PC1) has been deemed unusable for the algorithm's training purpose as it was found to represent variability in the signal intensity, which may be affected by the laser intensity noise and scattering volume fluctuations and thus, it is a less reliable characteristic of the sample's properties [14]. Additionally, Xiang *et al* have emphasized the difficulty in interpretation of PCA results applied to Brillouin scattering data that are associated with: (i) coarse resolution of Brillouin imaging and consequent spectral mixing of multiple components within a single imaging voxel and (ii) the method's sensitivity to spurious features such as the laser intensity fluctuations and its frequency drift [7]. Overall, PCA was found to be a sub-optimal method for spectral unmixing and signal processing of Brillouin imaging data compared to other supervised and unsupervised techniques [7].

In this article, we demonstrate that PCA is a simple and valuable method for understanding complex Brillouin scattering data collected from heterogeneous biological samples. By gradually increasing the sample complexity—from a water-plexiglass interface, to hydrogel spheroid and, finally, to a single cell (see figure 1)—we are able to explain most features of the PCA functions and assess the method's resilience against possible problems in data quality. We give step-by-step guidance for data pre-processing techniques that we believe are necessary to improve the outcomes of PCA method. Finally, we propose a new scheme in which PCA is combined with *k*-means clustering to enable spectral reconstruction and unmixing of Brillouin scattering data.

2. Methods

2.1. Sample choice

Three types of samples were used to carry out our study: (1) a plexiglass immersed in DI water, (2) a hydrogel spheroid in water and (3) human fibroblast cells. The choice of these three samples is motivated by the increasing level of complexity from sample 1 to 3 (see figures 1(a)–(c)). For example, sample 1 has two well-defined components (water and plexiglass) with distinctly different Brillouin frequencies ($\nu_W = \Omega_W/2\pi \approx 5.5$ GHz and $\nu_P = \Omega_P/2\pi \approx 11$ GHz) as schematically illustrated in figure 1(d). The hydrogel spheroid immersed in water undergoes a swelling process that results in a non-uniform distribution of the mechanical properties across it. Additionally, the Brillouin frequency of hydrogel ($\nu_H = \Omega_H/2\pi \approx 5.8$ GHz) is quite close to that of surrounding water, resulting in a spectral line overlap (figure 1(e)). Finally, a cell exhibits many intracellular components, each characterised by its frequency shift and linewidth, but overall closely spaced, leading to a complex asymmetric lineshape of the Brillouin scattered light (see figure 1(f)). Such a sample selection helps us understand the features of PCA method applied first to data collected from a simple sample, and then translate this knowledge to more complex scenarios.

2.2. Sample preparation

2.2.1. Hydrogel fabrication

2-Hydroxyethyl cellulose (average MW 380 000) was purchased from Sigma Aldrich. The HEC hydrogel was created by adding water to the HEC polymer (20% w/v). The mixture was vigorously stirred for 40 min to create a homogeneous solution and left to set. When the gel was still liquid, it was poured into the desired disk mould to complete its formation. The crosslinked hydrogel was checked under the wide-field microscope for any inconsistency in structure and moved to a sealed container for storage to prevent dehydration. The hydrogel disk was immersed in water for 1 h prior the measurements to equalize the hydration level.

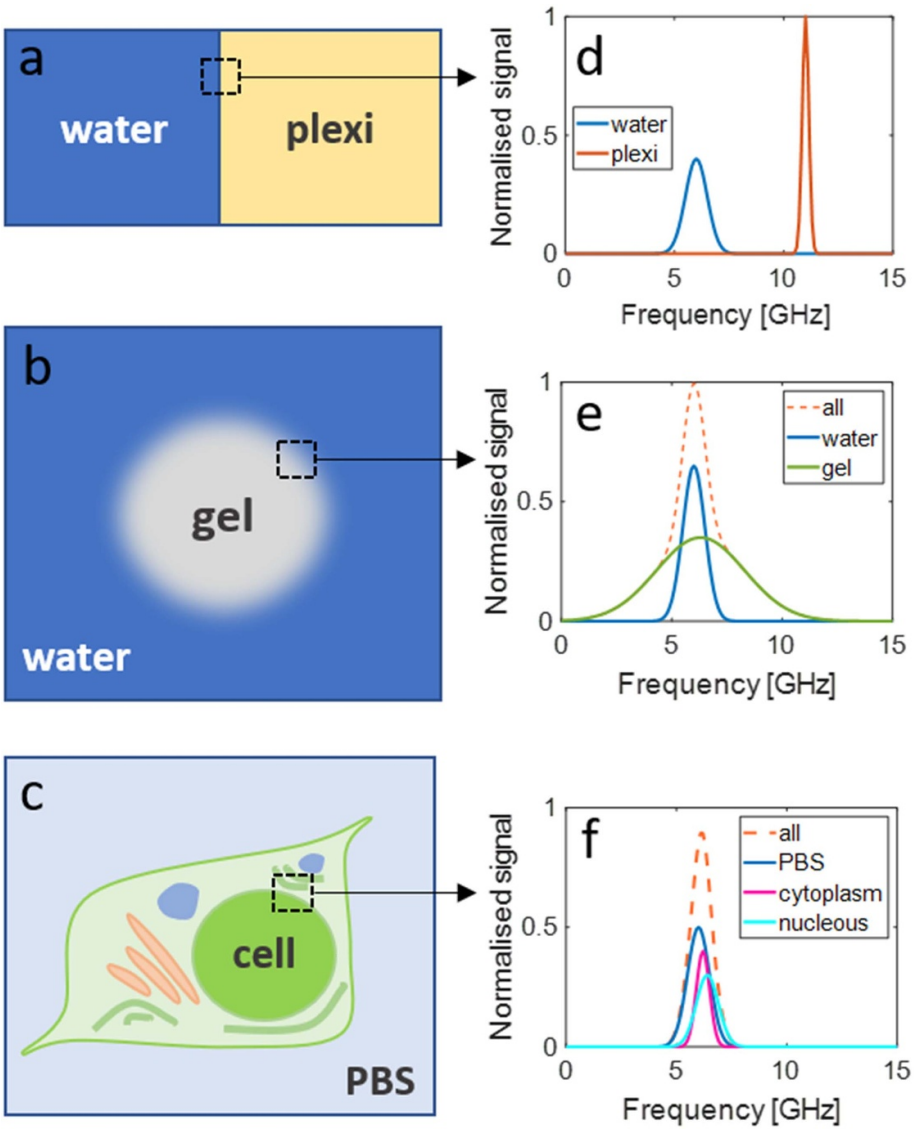

Figure 1. Schematic depiction of the three sample types: (a) water and plexiglass interface, (b) hydrogel spheroid in water and (c) a eukaryotic cell. The black box indicates the region where a few material components within each sample are present. The associated Brillouin spectra for anti-Stokes peaks are schematically shown in (d), (e) and (f), respectively.

2.2.2. Human fibroblast cells

A healthy human lung fibroblast cell line, MRC-5 (ATCC CCL-171) was purchased from American Type Cell Culture Collection (ATCC) and incubated at 37 °C with 5% CO_2. The cell line was cultured in Modified Eagle Medium (Gibco) supplemented with 10% (v/v) heat-inactivated foetal bovine serum (Invitrogen), 7.5% (v/v) sodium bicarbonate (Gibco), 1mM sodium pyruvate (Gibco) and 1% (v/v) non-essential amino acids (Sigma-Aldrich). MRC-5 cells were seeded in 6-well plates (Corning Costar) coated with fibronectin (2 $\mu g\,cm^{-2}$; Sigma-Aldrich) at a density of 4×10^4 cells cm^{-2}. The plates were washed with Phosphate Buffered Saline (PBS) to remove unadhered cells 72 h after seeding and fixed for 10 min at room temperature using 4% (v/v) paraformaldehyde/PBS. The MRC-5 cells were washed again then treated with PBS supplemented with 1% (v/v) Antibiotic-Antimycotic solution (Sigma-Aldrich).

2.3. Measurement system

The system employed for collecting spontaneous Brillouin scattering spectra consisted of a confocal microscope integrated with a specialized Brillouin spectrometer, utilizing a 6-pass tandem scanning Fabry–Perot interferometer (TFP1, tableStable Ltd). Sample illumination was achieved using a continuous frequency laser (660 nm, 120 mW, Torus, Laser Quantum) coupled to the confocal microscope (CM1, tableStable Ltd) and focused onto the sample using a microscope objective (20X Mitutoyo Plan Apo infinity corrected objective, NA = 0.42, WD = 20 mm, and 60X Nikon CFI APO NIR Objective, 1.0 NA, 2.8 mm WD). Subsequently, the light scattered in the backward direction was collected by the same objective lens and

directed to the 6-pass scanning Fabry–Perot interferometer for analysis. The spectral resolution of the Brillouin microscopy system is determined by the distance between the mirrors of the Fabry–Perot scanning interferometer (5 mm) and the number of acquisition channels (512), approximately equalling 276 MHz. The spectral extinction ratio of Fabry–Perot interferometers exceeds 10^{10} [15]. Spatial resolution is primarily influenced by the objective lens, potential aberrations within the confocal microscope, and spectrometer properties (input and output apertures). Considering these factors, our system's spatial resolution is estimated to be approximately 2 μm $\times$ 2 μm $\times$ 100 μm and 0.5 μm $\times$ 0.5 μm $\times$ 10 μm in the $X-Y-Z$ directions for 20X and 60X objective lenses, respectively. The Brillouin data collection utilized in-house software for two-dimensional (2D) scans within a sample plane, offering an acquisition time of 1–20 s per point depending on the sample transparency. To prevent sample damage from incident radiation, laser power was maintained below 20 mW. Raw spectra of Brillouin scattered light, containing Rayleigh and Brillouin peaks (Stokes and anti-Stokes), were fitted using the damped harmonic oscillator (DHO) model, where the peak positions determine the BFS.

2.4. Data pre-processing

2.4.1. Data signal-to-noise-ratio affects PCA outcomes

The signal-to-noise ratio (SNR) of Brillouin data depends on many factors, but can be controlled via reducing or increasing the time interval over which the signal is acquired at every spatial location within the sample (the acquisition time). In most experiments there exists a trade-off between selecting a suitable acquisition time (to achieve a sufficient SNR) and keeping scan times to a reasonable duration. We note that the percentages of each principal component found in the data set are not fixed, but depend on SNR (see correlation between the percentage of data explained by the first principal component, PC1, as a function of SNR for DI water measurements shown in supplementary information figure S2). More information on the role of SNR in processing of Brillouin data and the numerical techniques for noise reduction can be found elsewhere [16].

2.4.2. Data normalisation and spectral drift correction

In BM experiments there are a few measurement artefacts that can modify Brillouin spectra and which must be corrected to avoid the PCA algorithm identifying these as sample' characteristic features (see the results of PCA on non-normalised data in figure S3). The first effect is the variation in the absolute intensity of the spectral peaks at different spatial positions across the sample. These can occur due to the laser intensity fluctuations over the measurement time and the presence of reflective/scattering interfaces along the optical path. We corrected for this intensity fluctuations by normalising the spectral amplitudes. Specifically, we scaled each measured spectrum linearly to lie between the values of 0 and 1 over the frequency range of interest (between 4 and 8 GHz for biological media and between 9 and 13 GHz for plexiglass) by dividing the spectra by respective Brillouin peak maximum. Note that in highly scattering media, low-frequency spectral components associated with multiple scattering phenomenon may present a challenge for normalisation procedure and would need to be removed separately [17].

The second important extraneous effect is spectral drift, which is a common feature in Brillouin scattering spectroscopy and microscopy that originates from small changes in the laser wavelength over the duration of the experiment or long-term drifts in the optical system. Such drifts, if undetected and corrected, can result in errors for the parameters of interest, namely the Brillouin frequency shift, and thus need to be accounted for. To correct for spectral drift we recentre each spectrum to the average frequency value corresponding to the Stokes and anti-Stokes peaks.

We used self-written codes in Matlab to perform data pre-processing and plotting, whereas Matlab in-built functions were used for the principal component analysis and *k*-means clustering.

3. Analysis of Brillouin data from a water/plexiglass sample

To demonstrate the different steps of the analysis, we first consider Brillouin spectra from a sample consisting of a plexiglass slab immersed in water (figures 1(a) and 2(a)). The approximate height of the water layer was 1.5 cm, and that of the plexiglass rectangular slab was 1 cm, thus the glass was completely immersed in water from all sides. The measurement region consisted of a smaller 2D area of dimensions 1.65 mm $\times$ 1.55 mm, with a step size of 0.05 mm, chosen across the interface between water and plexiglass in a horizontal plane. Each spectrum was taken with an acquisition time of 10 s.

3.1. PCA analysis of Brillouin spectral data

Figure 2(a) shows the 2D sample region, for which each pixel in this 2D map represents the Brillouin frequency shift at specific spatial location, computed using a Damped Harmonic Oscillator model to fit the

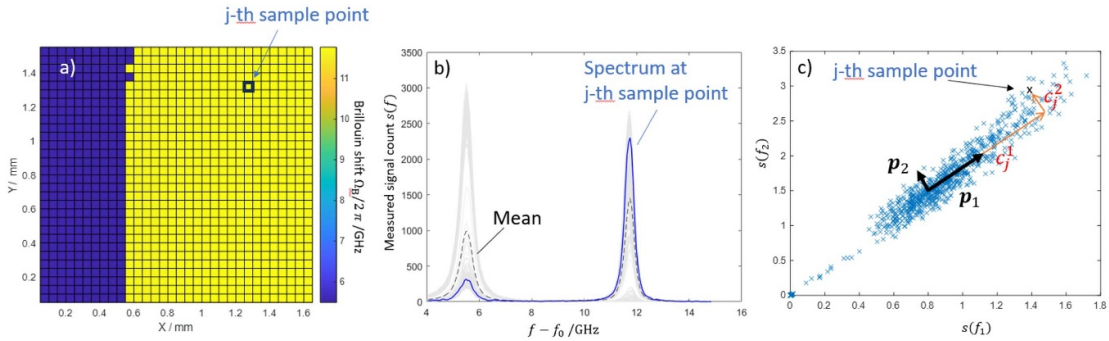

Figure 2. Brillouin spectral data collected from a sample containing plexiglass and water. (a) Map of the Brillouin frequency shift across the sample, as determined by fitting the data with DHO model. (b) Non-normalised spectral data as a function of frequency for all points in the domain, showing the mean (black dashed) and spectrum for an arbitrary single point within the sample (blue solid). The peaks for water (near 5.7 GHz) and plexiglass (near 11.8 GHz) are clearly visible. (c) Illustration of the correlation of spectral strength for two frequency points. The two-dimensional projections of the principal components are shown; each measured data point can be represented as a combination of the principal components.

spectral data. We observe clear separation between the two sample materials, with water ($\nu_W = \Omega_W/2\pi = 5.5\pm0.01$ GHz) on the left side and plexiglass ($\nu_P = \Omega_W/2\pi = 11.8\pm0.01$ GHz) on the right side. Both values agree reasonably well with the previously reported, albeit for a different measurement system and temperature [18, 19]. The raw non-normalised spectra at all points are shown in figure 2(b) with the black dashed line showing the mean spectrum calculated across the entire data set. As the scanning plane was chosen just slightly below the plexiglass surface, both water and plexiglass components appear at every measurement point on the plexiglass side of the sample.

We now perform PCA on the full spectral data set to identify the main spectral features without using a fitting model. If there are $n = N_x N_y N_z$ pixels in the Brillouin measurement volume, each of which yields a spectrum with m frequency bins, then we can represent the data set obtained from Brillouin measurement in the form of a $(n \times m)$ matrix $\mathbf{X}$; the rows of $\mathbf{X}$ then correspond to different observations (which represent different physical positions within the sample), and the columns correspond to the variables being observed (which represent the different frequencies of spectrum). The central idea of PCA is to use a linear transformation $\mathbf{P}$ to change the data set to a new $(n \times m)$ matrix

$$\mathbf{Y} = \mathbf{X}\mathbf{P}\,, \tag{1}$$

which is better at capturing the full variance of the data —specifically, $\mathbf{P}$ should be chosen to diagonalise the $(m \times m)$ covariance matrix of $\mathbf{Y}$

$$\mathbf{S}_\mathbf{Y} = \frac{1}{n-1}\mathbf{Y}^T\mathbf{Y}\,. \tag{2}$$

This occurs when the columns of $\mathbf{P}$ are equal to the eigenvalues of $\mathbf{S}_\mathbf{Y}$. Such a diagonalisation is usually performed using Singular Value Decomposition, but of course in-built packages for performing PCA are available on all the major programming platforms.

The columns of the coordinate transformation $\mathbf{P}$ are known as the principal components (PCs). The PCs represent the directions in an m dimensional space in which the variance of the data is maximized (see figure 2(c)), and so each principal component can be thought of as representing a particular piece of information associated with the measurement. Each PC of Brillouin data is a vector of length m and so is, effectively, a function of frequency. It is therefore tempting to associate each principal component with a particular material in the measured sample. However, this can lead to confusing results, especially since the resulting 'spectra' can have multiple peaks, and even be negative. Instead, it should be noted that the principal components represent departures from the *mean* spectrum as measured over all observations. The measured spectrum for the ith observation is given in terms of the PCs by

$$\mathbf{y}_i = \bar{\mathbf{y}}_i + \sum_{j=1}^{m} c_{ij}\mathbf{p}_j. \tag{3}$$

where the vector constants c_{ij} represent the *scores* (sometimes referred to as *abundances*) of the jth PC for the ith observation. The sum in equation (3) is usually truncated to include the smallest number of PCs that are able to explain the variance.

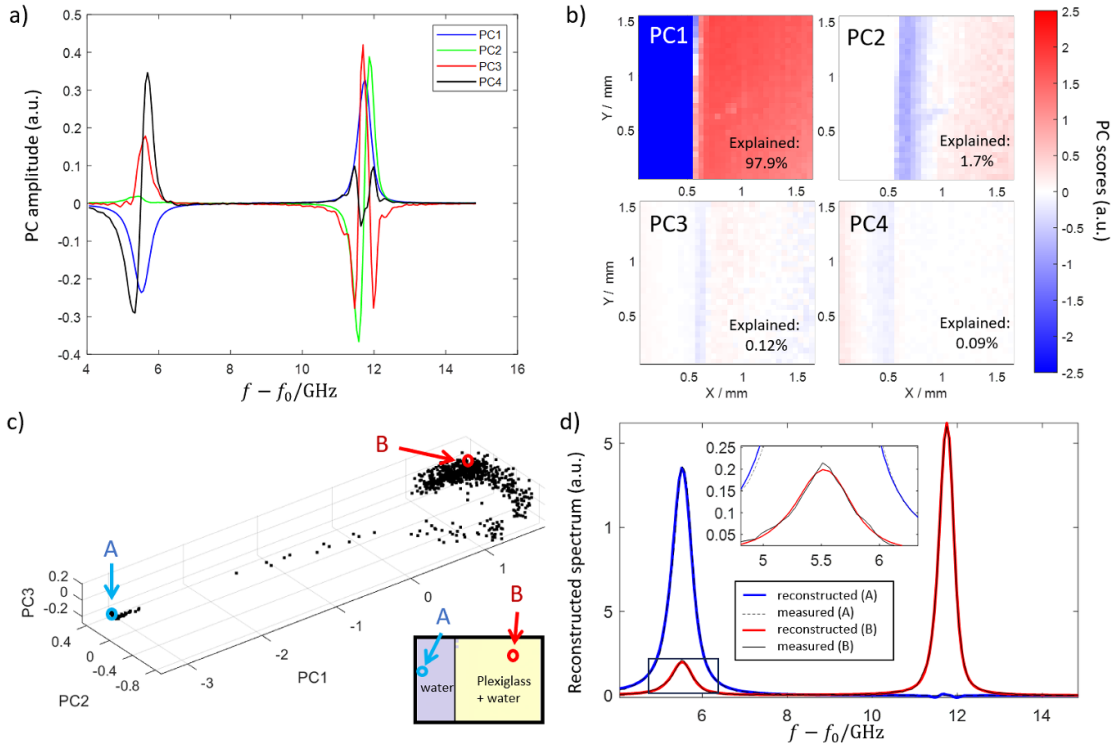

Figure 3. Principal components computed from Brillouin microscopy data from the plexiglass sample (see figure 1(a). (a) Spectral amplitude of the first three PCs. The Brillouin peaks are associated with strong variations in each of the PCs. (b) Mapping across the sample of the scores of the first four PCs. (c) The scores of the first three PCs plotted against each other. Similar materials, giving rise to similar spectra, can be seen to cluster together. The point *A* is located entirely within the water layer, while the point *B* is located within the plexiglass/water layer. (d) Reconstructed spectra at the points *A* and *B* using the first three PCs. The reconstruction fits the measured spectrum at these data extremely closely; differences can be seen when zooming in to the graph (insert).

According to equation (3), each data point can be represented as a combination of PCs, which in turn represent the direction of greatest variance in the data. This is graphically shown in figure 2(c), which shows the decomposition of the measured spectra at two specific frequencies into the first two principal components. Here the black vectors represent the principal components $\mathbf{p}_1$ and $\mathbf{p}_2$, with the scores of the jth sample point for these first two PCs shown in red.

The PC amplitudes (for the first three components) for the water/plexiglass sample are shown in figure 3(a). We note that these spectral functions are multi-peaked and negative—this is a consequence of the fact that they represent variations in the data with respect to the mean measured spectral values. The scores for the first four PCs are shown as a map across the sample region in figure 3(b): here each score represents the amplitude of the given PC at the corresponding spatial location. We use a red-blue colour scheme for which white represents a score of zero. The difference between the regions, as well as the edge of the water/plexiglass layer, is visible in the first four components. It can be seen that the PC scores decrease (become more 'white') for higher order PCs.

3.2. Extraction of spectra and identification of materials

The main goal of PCA is to identify the spectra of different materials in the sample region. While the PCs contain information that describes the greatest variation in the data, it is important to keep in mind that this variation may not correlate with the underlying spectrum. For example, even after normalisation, the measurement may have a uniform drift in amplitude across the sample volume. Another problem that frequently occurs in Brillouin microscopy is that measurements of two different materials (say, water and cell cytoplasm) may occur within the same observation; this makes the distinction between the spectra challenging.

We can extract the underlying material spectra by noting that similar materials should possess similar PC scores because the spectrum of each constituent material is the same. We then expect that observations of the same material will cluster together in the m-dimensional space of PCA scores. If only two (or three) PCs are needed to explain the data, then the observations of a given material will cluster together in two (or three) dimensions. We observe this clustering in figure 3(c). From the spatial distribution of data points we observe that the majority of points aggregate near the region labelled with *B*, with another cluster formed at the

opposite end of the PC-space around point *A*. If we then examine the spatial locations of points *A* and *B*, we find that *A* is located entirely inside water whereas the *B* is within the plexiglass. We can confirm this by reconstructing the spectra at points *A* and *B* using equation (3); the results are shown in figure 3(d), and show a peak near 5.7 GHz for the point *A* and a high-amplitude peak near 11.8 GHz for point *B*. We note also that the reconstructed spectra are extremely close to the measured spectra, demonstrating that the first 3 PCs are sufficient to explain the measured data to visual accuracy.

3.3. Clustering and unsupervised separation of materials

Proceeding from the observation that clusters in PC space correspond to different materials, we now seek an unsupervised method for separating these clusters and thus identifying regions containing different materials in the sample. A straightforward method to achieve this is *k*-means clustering, in which the clusters are classified according to the squared Euclidean distance to the nearest mean of the cluster group [20]. *K*-means clustering is an unsupervised method for which the number of clusters must be specified as input to the algorithm. It is therefore straightforward to implement if the number of clusters is known, as in the water/plexiglass sample. However, without preliminary knowledge of the sample properties, it can be difficult to pinpoint the specific number of clusters that carry physically relevant information. Therefore, to identify the number of clusters in the sample we combine the *k*-means algorithm with the *knee method* (also known as the *elbow method*). In this method, the number of clusters *K* is increased until the Within-Cluster-Sum of Squares (WCSS) value reaches a 'knee point', which is the point of maximum curvature on the WCSS-*K* curve. For a discrete, noisy set of points this point can be located using the Kneedle algorithm of Satopaa *et al* [21], which smoothies and normalises the WCSS-*K* curve to find the point of maximum curvature; because this point typically falls between two integers, we choose the number of clusters to be one integer above that predicted by the Kneedle algorithm. We note also that care must be taken in implementing the Kneedle algorithm that a sufficiently high range of clusters is tested: the algorithm will converge to the correct inflection point ('knee') as the number of number of clusters increases.

We show the WCSS curve for different numbers of clusters in figure 4(a). The position of the 'knee', as given by the Kneedle algorithm, is between clusters 2 and 3, indicating the optimal number of clusters as 3. In figure 4(b)) we show the grouped clusters in PC space—one can see the two clusters corresponding to water (blue) and plexiglass/water (red) have been correctly grouped together by the *k*-means algorithm, together with a sparse collection of points (green) connecting them. These points form a third cluster along the interface between the two layers. We can see this by mapping the cluster number of each point to its physical location: in figure 4(c) one can see that the different clusters correspond to regions of water, plexiglass, and the thin interface between them. It is instructive that the interface region does not contain new frequencies, as it would if it were comprised of a new material. Instead, the interface region is where the relative heights of the two main Brillouin peaks change rapidly. This results in a different combination of PC components, which is identified as a distinct group by the clustering algorithm.

A different clustering algorithm may divide the points in PC space in a different way: for example, one can see in figure 4(b)) a section of the plexiglass cluster (red) that is slightly separated from the main cluster, and for which a different clustering algorithm may allocate to a different or its own cluster (for this example these correspond to points near the interface on the plexiglass side). To separate these points one could use a more sophisticated algorithm (such as DBSCAN), or resort to supervised division of the clusters [22].

4. Analysis of Brillouin data from a hydrogel spheroid

We now repeat the same procedure for the second sample (see figure 1(b)), a hydrogel spheroid. The fitted Brillouin frequency map is shown in figure 5(a). The WSCC values are shown in figure 5(b), and identify 3 clusters, which are represented in PC space for the first three PCs in figure 5(c). Here the clusters are not noticeably distinct, forming a continuous spread in PC space. We hypothesize that the swelling process leads to non-uniform distribution of the mechanical properties, forming a core–shell structure with a stiffer core in the middle of the spheroid and softer, more hydrated shell around it.

We plot a representative spectrum for each of the three clusters by selecting the central point in each cluster (solid lines in figure 5(d)) and compare this to spectral functions reconstructed for the points *A*, *B* and *C* taken within each of the cluster group. We observe good agreement between the reconstructed spectral lines and the spectrum derived at the centre of the corresponding cluster. The identified regions are shown in figure 5(e), where the three clusters correspond to the interior, boundary and exterior of the spheroid. Finally, we can obtain the Brillouin frequency shift and Brillouin linewidth at the centre of each cluster independently; the results are shown in the table of figure 5(f). As expected, the Brillouin frequency shift is

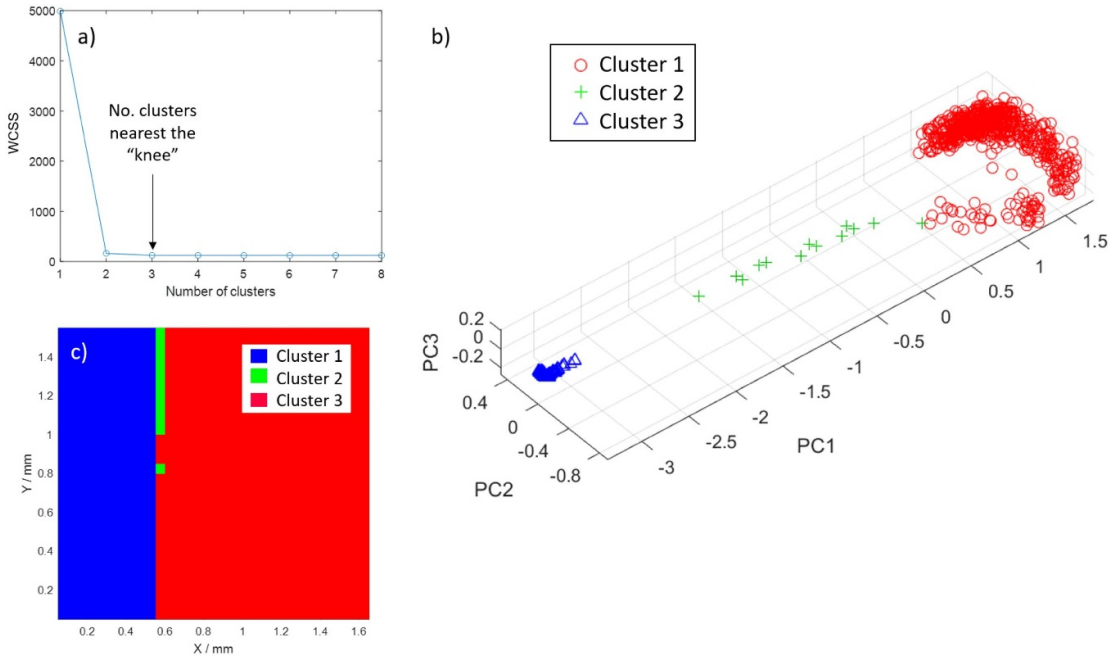

Figure 4. Clustering analysis of the PC scores for the water/plexiglass sample. (a) Computed Within-Cluster Sum of Squares (WCSS) for different numbers of clusters. The point closest to the 'knee' is at 3 clusters. (b) Plot of PC scores grouped into three clusters, which can be associated with water (blue), plexiglass/water (red) and a boundary region (green). (c) Mapping of the three cluster regions across the sample.

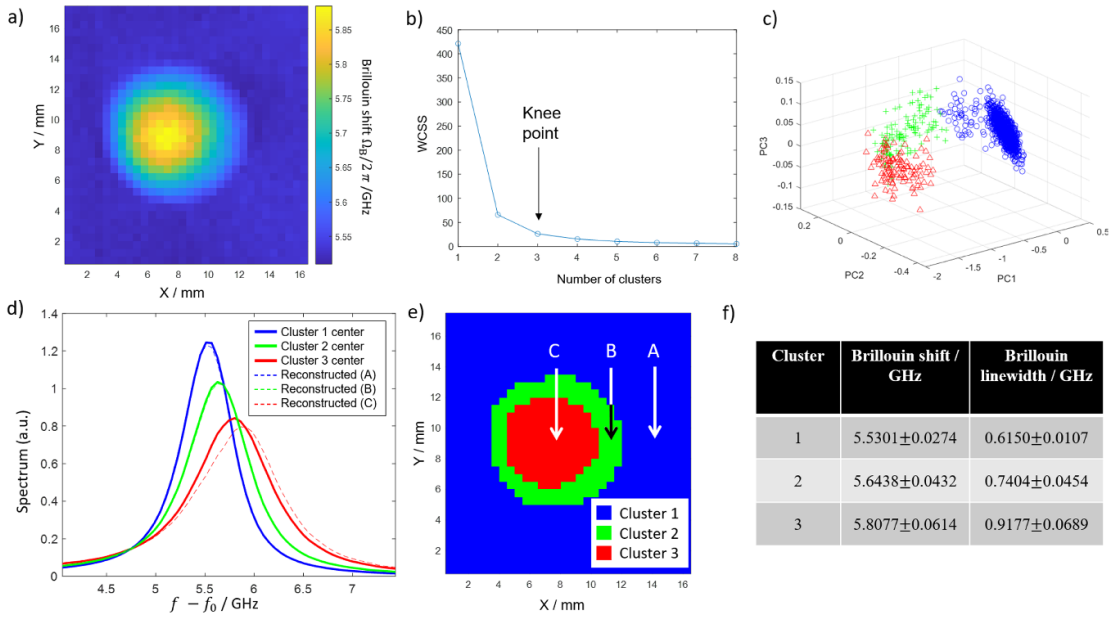

Cluster	Brillouin shift / GHz	Brillouin linewidth / GHz
1	5.5301±0.0274	0.6150±0.0107
2	5.6438±0.0432	0.7404±0.0454
3	5.8077±0.0614	0.9177±0.0689

Figure 5. PCA and clustering for the hydrogel sample (compare to figure 1(b)). (a) Mapping of BFS across the sample. (b) Clustering analysis of PC scores, with knee point computed at 3 clusters. The explained variance for the first three PCs is 95.8% (PC1), 2.86% (PC2) and 0.23% (PC3). (c) PC scores for the first three PCs, divided into three clusters. (d) Brillouin spectrum at the mean point of each cluster, compared with the reconstructed spectrum at points at the very centre of the hydrogel sample (A), on the boundary of the sample (B) and within the exterior region (C). Both BFS and linewidth increase toward the centre of the hydrogel. (e) Mapping of the cluster groups in the different parts of the sample. The points *A*, *B* and *C* show the points for the spectra in (d). (f) Computed BFS and linewidth at the centre of each cluster, using the spectra obtained from the first three PCs, as well as the standard deviation of these quantities over the whole of the cluster.

the largest in cluster 3, which corresponds to the spheroid core, while reducing slightly for the shell structure at the spheroid's periphery. The linewidth also decreases as we move from the interior to the exterior of the spheroid.

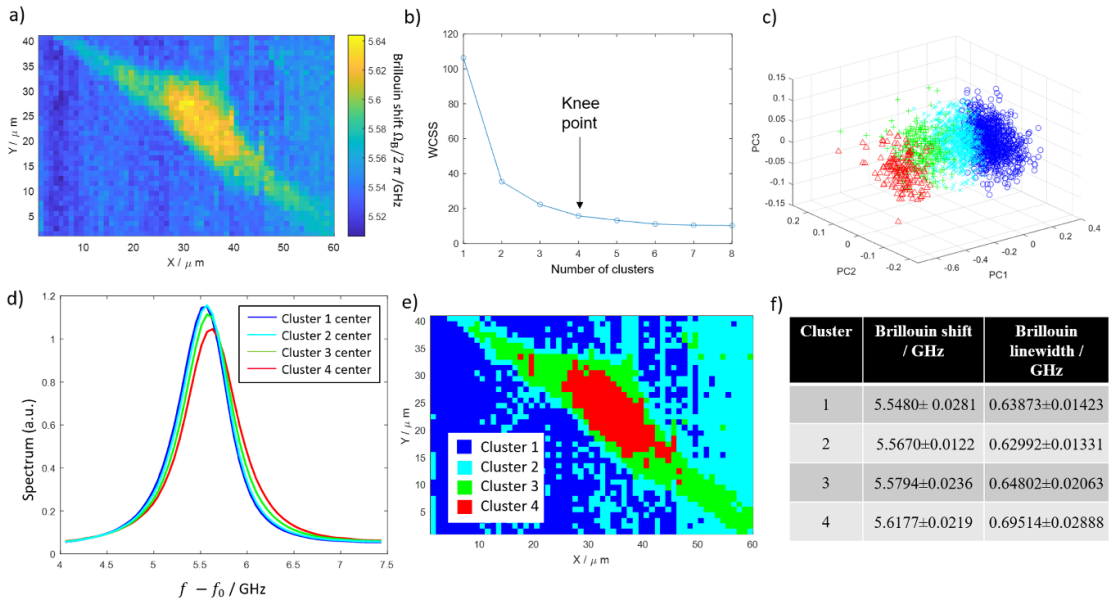

Cluster	Brillouin shift / GHz	Brillouin linewidth / GHz
1	5.5480± 0.0281	0.63873±0.01423
2	5.5670±0.0122	0.62992±0.01331
3	5.5794±0.0236	0.64802±0.02063
4	5.6177±0.0219	0.69514±0.02888

Figure 6. PCA and clustering for the human fibroblast cell (compare to figure 1(c)). (a) Mapping of BFS across the sample. (b) Clustering analysis of PC scores, with knee point computed at 4 clusters. (c) PC scores of the first three PCs, divided into four clusters. The explained variance for the first three PCs is 71.7% (PC1), 5.63% (PC2) and 2.55% (PC3). (d) Brillouin spectra computed at the central point of each cluster. (e) Mapping of the clusters in the different parts of the sample. (f) Computed BFS and linewidth at the centre of each cluster, using the spectra obtained from the first three PCs, as well as the standard deviation of these quantities over the whole of the cluster.

5. Analysis of Brillouin data from a human lung fibroblast cell

The spatial distribution of Brillouin frequency shifts in the third sample, an MRC fibroblast cell (see figure 1(c)), is depicted in figure 6(a). Higher BFSs are observed in the cell centre compared to the cell periphery. This suggests a larger longitudinal modulus associated with the cell centre, although this can only be confirmed if the distribution of the refractive index and mass density is known or can be measured in parallel with BFS detection [23]. The WSCC curve (figure 6(b)), identifies the knee point at four clusters, shown in PC space for the first three PCs in figure 6(c). As with the hydrogel sample, the PC scores form a continuum of points rather than distinct groups.

In figure 6(d), the Brillouin spectra for the centre of each cluster are plotted. These spectra exhibit slight variations in peak positions and intensities, which suggest differences in the mechanical properties between the regions. The regions corresponding to the different clusters are shown in figure 6(e). The cell centre is clearly visible, as is the outer layer corresponding to cell cytoplasm and membrane. The frequency shifts and linewidths of the cluster centres are tabulated in figure 6(f). These measurements indicate a range in material stiffness and structural heterogeneity across the clusters. We see that the Brillouin shifts and linewidths of the exterior region (Clusters 1 and 2) are very close, and may arise because the clustering approach is identifying differences between the immersion liquid, PBS, and the fibronectin layer on which the cells are seeded, which is much thinner (approx. 3–5 micron) than the axial spatial resolution.

6. Discussion

We now discuss our findings and compare how these align with the previously reported in the literature. First, we note that our main intention for this work was to provide a workflow guide to PCA method in application to Brillouin microscopy data. As mentioned previously, this method is still relatively underutilised with only a few reports available to date [7, 13, 24]. It is possibly due to this lack of use, many features of the method have not been previously explained. This could lead to misinterpretations and confusion by the research community, as well as rejection of the method altogether.

One of the features that have not been understood or interpreted correctly involves the functional form of the principal components. As discussed in section 3.1, these can become negative-valued and may be confusing to interpret as these PC functions do not always resemble the measured spectra. Once understood that the PC functions need to be viewed as variations from the 'mean' spectra and corrected accordingly, the true functional form of principal components can be reconstructed (figures 5(d) and 6(d)). Such reconstruction may be particularly valuable for analysing the data collected from Brillouin imaging of

heterogeneous materials such as cells. Most of the Brillouin imaging methods suffer from insufficient spectral resolution, with stimulated Brillouin imaging [25] and scanning Fabry–Perot [24] techniques achieving the best resolution to date (approx. 100 MHz). Similarity of the material components in a cell gives rise to the close position of different components' Brillouin peaks in the spectral domain, sometimes within a spectral bandwidth of 100–200 MHz (as in our cell sample) and similar to the instrument's resolution, leading to spectral overlaps between the features. Thus, direct observation and identification of material components often is not possible with the current level of technology. Hence, PCA or other supervised and unsupervised methods might present the only solution to disentangle the complex spectral data collected from heterogeneous samples.

In this work we have presented a new method in which PCA is coupled with *k*-means clustering to assist with data interpretation. We see this as a complimentary approach, that is particularly valuable in situations where large volumes of data need to be processed fast, without preliminary knowledge of the sample structure and content. In that specific situation, the discretization of all data into clusters, that can be analysed separately and compared statistically against different control and treatment groups, can provide the means for rigorous and unbiased analysis in which no *a priory* knowledge of the spectral line-shape is needed. In fact, the spectra collected from complex samples such as cells cannot be fitted well with a single peak line-shape functions such as Lorentz (symmetric) or Damped Harmonic Oscillator (asymmetric) models, as these give rise to inaccurate results and lead to misinterpretation of the measured data. To illustrate this point we applied *k*-means clustering analysis to our fibroblast cell data directly, without processing it first with PCA (see supplementary information figure S4). Depending on the model used, one can notice about 30 MHz difference in the average Brillouin frequency shift for each cluster. This difference clearly is the result of the model choice rather than physical properties of the sample, and hence represents data processing artefact. Closer look at the clusters' boundaries also suggests fitting-model-dependent differences in association of individual pixels with a certain cluster number (see figures S4(a) and (b)).

We note however, that for many sample types, including cells and non-uniform biomaterials such as hydrogels as shown in this article, the Brillouin spectral signatures represent a continuum rather than naturally discrete data. This is evident from the PC space for our hydrogel and cell samples (figures 5(c) and 6(c)). Thus, any division of the data into artificially created bins may lead to errors, especially for data points at the boundary between any two neighbouring clusters. The knee (elbow) method is a good tool to assess the cluster number and avoid 'over-binning' of the data. However, it does not resolve the more conceptual conflict between the discrete and continuum nature of spectral information and potential risk assigning the wrong labels to a small number of data points. Depending on the data set volumes and the tasks at hand, the risk of error might be fairly insignificant when weighted against the benefits of the clustering method.

Similarly to the reports by Xiang *et al* [7, 16], we identified the value of data pre-processing techniques to enhance the performance of PCA method. Data spectral alignment and normalisation are the main procedures that need to be considered. We confirmed that the quality of the analysis and the distribution of the PC scores are heavily dependent on these pre-processing steps. Surprisingly, we also found that the scores of the principal components were dependent on the data signal to noise ratio (see supplementary information). This suggests that PCA method might not be the best option for the analysis of low SNR data collected with VIPA-based spectrometers where the imaging speed has been prioritised over the signal quality. Failure to correct for imaging artefacts such as frequency drifts coupled with low SNR data may indeed lead to PCA method producing spurious features devoid of physical meaning, and should be avoided.

7. Conclusion

In conclusion, we discussed the application of principle component analysis of data collected from Brillouin microscopy experiments and provided the guide to data workflow, including pre-processing steps to improve data quality and data transformation into principle components and clusters. For large sets of data (hundreds to thousands of spectra) PCA presents significantly faster method compared to spectral line fitting (fractions of a second compared to minutes). Additionally, PCA does not require any preliminary knowledge of the sample composition, structure, nor guesses of a suitable line shape model. This presents a significant advantage when dealing with complex, heterogeneous samples, for which a single line shape fitting typically results in a significant error. Additionally, we have proposed a combination of PCA with a *k*-means clustering method that we believe is particularly suitable for biological and biomedical studies with high sample throughput and the need for statistical analysis across various sample groups.

Data availability statement

The data that support the findings of this study will be openly available following an embargo at the following URL/DOI: https://profiles.uts.edu.au/Irina.Kabakova. Data will be available from 01 May 2024.

Acknowledgments

The authors acknowledge the support by the Australian Research Council Centre of Excellence in Optical Microcombs for Breakthrough Science (CE230100006) and the Australian Research Council Centre of Excellence in Quantum Biotechnology (CE230100021).

ORCID iD

Irina V Kabakova https://orcid.org/0000-0002-6831-9478

References

[1] Palombo F and Fioretto D 2019 Brillouin light scattering: applications in biomedical sciences *Chem. Rev.* **119** 7833–47
[2] Poon C, Chou J, Cortie M and Kabakova I 2020 Brillouin imaging for studies of micromechanics in biology and biomedicine: from current state-of-the-art to future clinical translation *J. Phys. Photon.* **3** 012002
[3] Yakovlev V 2016 Seeing cells in a new light: a renaissance of Brillouin spectroscopy *Latin America Optics and Photonics Conference* (Optica Publishing Group) p LTh3A.7
[4] Wu P-J, Masouleh M I, Dini D, Paterson C, Török P, Overby D R and Kabakova I V 2019 Detection of proteoglycan loss from articular cartilage using Brillouin microscopy, with applications to osteoarthritis *Biomed. Opt. Express* **10** 2457–66
[5] Polonchuk L *et al* 2021 Towards engineering heart tissues from bioprinted cardiac spheroids *Biofabrication* **13** 045009
[6] Mahmodi H, Piloni A, Utama R H and Kabakova I 2021 Mechanical mapping of bioprinted hydrogel models by Brillouin microscopy *Bioprinting* **23** e00151
[7] Xiang Y, Seow K L C, Paterson C and Török P 2021 Multivariate analysis of Brillouin imaging data by supervised and unsupervised learning *J. Biophoton.* **14** e202000508
[8] Wu P, Kabakova I V, Ruberti M, Sherwood J M, Dunlop I E, Paterson C, Török P and Overby D R 2018 Water content, not stiffness, dominates Brillouin spectroscopy measurements in hydrated materials *Nat. Methods* **15** 561–2
[9] Randleman J B, Zhang H, Asroui L, Tarib I, Dupps W J and Scarcelli G 2023 Subclinical keratoconus detection and characterization using motion-tracking Brillouin microscopy *Ophthalmology* **131** 310–21
[10] Shlens J 2014 A tutorial on principal component analysis *Educational* **51** 1–9
[11] He X, Liu Y, Huang S, Liu Y, Pu X and Xu T 2018 Raman spectroscopy coupled with principal component analysis to quantitatively analyze four crystallographic phases of explosive CL-20 *RSC Adv.* **8** 23348–52
[12] Masia F, Glen A, Stephens P, Borri P and Langbein W 2013 Quantitative chemical imaging and unsupervised analysis using hyperspectral coherent anti-stokes Raman scattering microscopy *Anal. Chem.* **85** 10820–8
[13] Palombo F, Masia F, Mattana S, Tamagnini F, Borri P, Langbein W and Fioretto D 2018 Hyperspectral analysis applied to micro-Brillouin maps of amyloid-beta plaques in Alzheimer's disease brains *Analyst* **143** 6095–102
[14] Cardinali M A, Morresi A, Fioretto D, Vivarelli L, Dallari D and Govoni M 2021 Brillouin and Raman micro-spectroscopy: a tool for micro-mechanical and structural characterization of cortical and trabecular bone tissues *Materials* **14** 6869
[15] Sandercock J 1976 Simple stabilization scheme for maintenance of mirror alignment in a scanning February-Perot interferometer *J. Phys. E: Sci. Instrum.* **9** 566
[16] Xiang Y, Foreman M R and Török P 2020 SNR enhancement in Brillouin microspectroscopy using spectrum reconstruction *Biomed. Opt. Express* **11** 1020–31
[17] Mattarelli M, Capponi G, Passeri A A, Fioretto D and Caponi S 2022 Disentanglement of multiple scattering contribution in Brillouin microscopy *ACS Photon.* **9** 2087–91
[18] Scarcelli G and Yun S-H 2008 Confocal Brillouin microscopy for three-dimensional mechanical imaging *Nat. Photon.* **2** 39–43
[19] Scarcelli G, Polacheck W J, Nia H T, Patel K, Grodzinsky A J, Kamm R D and Yun S H 2015 Noncontact three-dimensional mapping of intracellular hydromechanical properties by Brillouin microscopy *Nat. Methods* **12** 1132–4
[20] Ikotun A M, Ezugwu A E, Abualigah L, Abuhaija B and Heming J 2023 K-means clustering algorithms: a comprehensive review, variants analysis and advances in the era of big data *Inf. Sci.* **622** 178–210
[21] Satopaa V, Albrecht J, Irwin D and Raghavan B 2011 Finding a' kneedle' in a haystack: detecting knee points in system behavior *31st Int. Conf. on Distributed Computing Systems Workshops* (IEEE) pp 166–71
[22] Ester M, Kriegel H-P, Sander J and Xu X 1996 A density-based algorithm for discovering clusters in large spatial databases with noise *Proc. of 2nd Int. Conf. on Knowledge Discovery and Data Mining* vol 96 pp 226–31
[23] Schlüßler R *et al* 2022 Correlative all-optical quantification of mass density and mechanics of subcellular compartments with fluorescence specificity *eLife* **11** e68490
[24] Cardinali M A *et al* 2022 Brillouin-Raman microspectroscopy for the morpho-mechanical imaging of human lamellar bone *J. R. Soc. Interface* **19** 20210642
[25] Remer I, Shaashoua R, Shemesh N, Ben-Zvi A and Bilenca A 2020 Shemesh, high-sensitivity and high-specificity biomechanical imaging by stimulated Brillouin scattering microscopy *Nat. Methods* **17** 913–6